Quantitative Relationship between Support Porosity and the Stability of Pore-Confined Metal Nanoparticles Studied on CuZnO/SiO_2 Methanol Synthesis Catalysts

Gonzalo Prieto, Mozaffar Shakeri, Krijn P. de Jong, and Petra E. de Jongh*

Inorganic Chemistry and Catalysis, Debye Institute for Nanomaterials Science, Utrecht University, 3584 CG, Utrecht, The Netherlands

ABSTRACT Metal nanoparticle growth represents a major deactivation mechanism of supported catalysts and other functional nanomaterials, particularly those based on low melting-point metals. Here we investigate the impact of the support porous structure on the stability of CuZnO/SiO_2 model methanol synthesis catalysts. A series of silica materials with ordered cagelike (SBA-16 mesostructure) and disordered (SiO_2-gel) porosities and varying pore sizes were employed as catalyst supports. Nitric oxide moderated nitrate decomposition enabled the synthesis of catalytically active Cu nanoparticles (3−5 nm) exclusively inside the silica pores with short interparticle spacings. Under relevant reactive conditions, confinement of the Cu particles in cagelike silica pores notably enhances catalyst stability by limiting Cu particle growth as compared to catalysts deposited in SiO_2-gel host materials with also 3D and highly interconnected though unconstrained porosity. For both pore morphologies, we find a direct relationship between catalyst stability and support porosity, provided the narrowest characteristic pore dimension is employed as a porosity descriptor. For cagelike porosities this corresponds to the size of the entrances to the nanocages. Our results point to nanoparticle diffusion and coalescence as a relevant growth mechanism under reactive conditions and underscore the significance of the narrowest pore constrictions to mitigate growth and improve catalyst stability. This finding contributes to the establishment of general and quantitative structure−stability relationships which are essential for the design of catalysts and related functional nanostructures with long lifetimes under operation conditions.

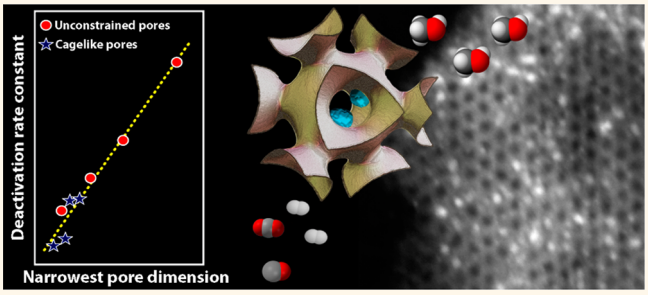

KEYWORDS: metal nanoparticles · porous materials · supported catalysts · pore morphology · stability · particle growth · sintering

Nanostructure materials containing supported metal nanocrystallites are essential functional materials for energy storage and conversion, electronics, plasmonics, and catalysis. However, the tendency of nanosized metal particles to grow into larger crystals under operation conditions stands out as a major challenge. For instance for catalysts,[1] particle growth, proceeding *via* either particle diffusion and coalescence or Ostwald ripening,[2] represents a major catalyst deactivation pathway.[3,4] Next to the decline in the metal surface area available for catalysis, particle growth can also result in deterioration of the activity and selectivity in applications where these properties depend strongly on the particle size[5−9] or by reducing the amount of catalytically relevant metal−support interface sites.[10−12]

Developing efficient and widely applicable strategies to stabilize supported metal nanoparticles under relevant operation conditions is hence a priority. Approaches which have been recently proposed include alloying,[13] optimizing the metal−support interaction,[14,15] encapsulation of individual nanoparticles in porous oxide shells,[16−18] and maximizing the interparticle spacings.[19,20] The porous structure of the support material is a crucial factor for catalyst stability.[21,22] Generally, narrow pores mitigate particle

* Address correspondence to P.E.deJongh@uu.nl.

Received for review November 27, 2013 and accepted February 10, 2014.

Published online February 10, 2014
10.1021/nn406119j

© 2014 American Chemical Society

growth, an effect which likely relates to lower particle mobility when the size of the growing nanoparticles becomes similar to that of the pore host.[23−25] Besides pore size, pore connectivity and morphology have been claimed to be important for particle growth. 1D porosities were suggested to limit growth as compared to highly interconnected, 3D pore systems, possibly by restricting the pathways for the transport of metal species.[19,26] However, 3D interconnected porosities are strongly preferred to avoid mass transport limitations and pore blockage.

Support materials with cagelike pore architecture represent outstanding candidates to study the impact of pore morphology on catalyst stability. Their pore structure consists of a 3D arrangement of nanocages interconnected *via* narrower entrances.[27−30] The cages can accommodate metal nanoparticles, while the cage entrances are expected to represent physical barriers to particle mobility and therefore counter particle coalescence. Recent studies have reported the incorporation of catalytic metal nanoparticles in cagelike porous supports.[31−33] Often, the synthesis strategies required the use of cosurfactants and/or organic capping agents to achieve small metal particles located exclusively inside the nanocages of the support material.[32,33] Although benefits for catalyst stability have been reported upon confinement of metal nanoparticles to cagelike pores,[31,32] the impact of cage and entrance sizes on catalyst stability has not been investigated to the best of our knowledge.

Catalysts based on (Zn-promoted) Cu nanoparticles are of industrial significance for a variety of processes such as selective hydrogenations, the water gas-shift reaction, and methanol synthesis from a mixture of H_2 and CO/CO_2 ("synthesis gas").[34,35] However, a major limitation is the intrinsic poor stability of the supported Cu nanoparticles,[19,36,37] which are prone to grow already at relatively low operation temperatures. Industrial $Cu/ZnO(Al_2O_3)$ catalysts are commonly manufactured by coprecipitation routes resulting in Cu nanoparticles within a disordered network of ZnO (and Al_2O_3) nanocrystallites.[38−40] Model SiO_2-supported CuZnO catalysts with well-defined nanostructures are particularly attractive to address fundamental aspects of catalyst activity and stability.[41−44]

Recently, we have reported how advanced control over the nanospatial distribution of metal nanoparticles on the support porosity represents a powerful approach to improve our understanding of catalyst stability under relevant reaction conditions.[19] Maximizing the interparticle distances results in improved catalyst stability, with Ostwald ripening likely being the dominant growth mechanism. For particles grouped in domains with high local metal loadings, representative of those often encountered in technical catalysts, migration and coalescence of neighboring nanoparticles play a significant role in growth. Hence, catalysts displaying small metal nanoparticles in close proximity represent ideal model systems to assess the impact of the size and morphology of the pores of the support material on particle growth and catalyst stability.

Here we study the impact of support porosity on the stability of $CuZnO/SiO_2$ methanol synthesis model catalysts. A simple, low-waste impregnation method with an aqueous metal nitrate solution enables the synthesis of pore-confined Cu nanoparticles (3−5 nm) with short interparticle spacings. Under industrially relevant reaction conditions, we directly compare the stability of catalysts confined to the cagelike pores of SBA-16 silica mesostructures to that of catalysts supported on SiO_2-gel carriers with unconstrained pores. The size of the nanocages and the connecting entrances in the SBA-16 support materials is systematically adjusted and quantified to determine its impact on catalyst stability.

RESULTS AND DISCUSSION

Porous Support Materials. SBA-16 silica consists of a body-centered-cubic arrangement of nanocages (generally 5−10 nm in diameter) connected to their nearest neighbors by entrances typically narrower than 5 nm.[27] The synthesis conditions were adjusted to prepare mesostructures with varying cage and entrance sizes. As revealed by SEM, the primary particles for all the SBA-16 silicas show a combination of spherical and polyhedral shapes with sizes ranging from 1 to 10 μm (Supplementary Figure S1). The porous structure of the SiO_2 supports was characterized by gas physisorption methods. Figure 1 shows the N_2-physisorption isotherms and the corresponding cage/pore size distributions for the series of SBA-16 and the commercial SiO_2-gel reference materials.

As judged from the abrupt closure of the hysteresis loop at $P/P_0 \approx 0.47$, cavitation is the major desorption mechanism for all SBA-16 mesostructures, precluding the quantitative analysis of the desorption branch.[45,46] The adsorption branches of the isotherms have been analyzed to derive the cage and pore size distributions for both series of SBA-16 and SiO_2-gel materials. As shown in Figure 1b, the SBA-16 mesostructures displayed narrow cage size distributions peaking in the range of 5−9 nm. Such pore uniformity results from their micelle-templated synthesis. Wider pore size distributions with mean pore diameters in the range of 4−15 nm were determined for the SiO_2-gel materials. Table 1 summarizes some key textural features of the support materials. For both series, the total pore volume increases on increasing the cage or pore diameter. SBA_5, with the smallest cage diameter, shows a significant micropore contribution, which is known to correspond to micropores within the silica pore walls.[27] Such intrawall microporosity becomes notably reduced ($\leq$7%) for SBA-16 silicas with wider cages, as a result of

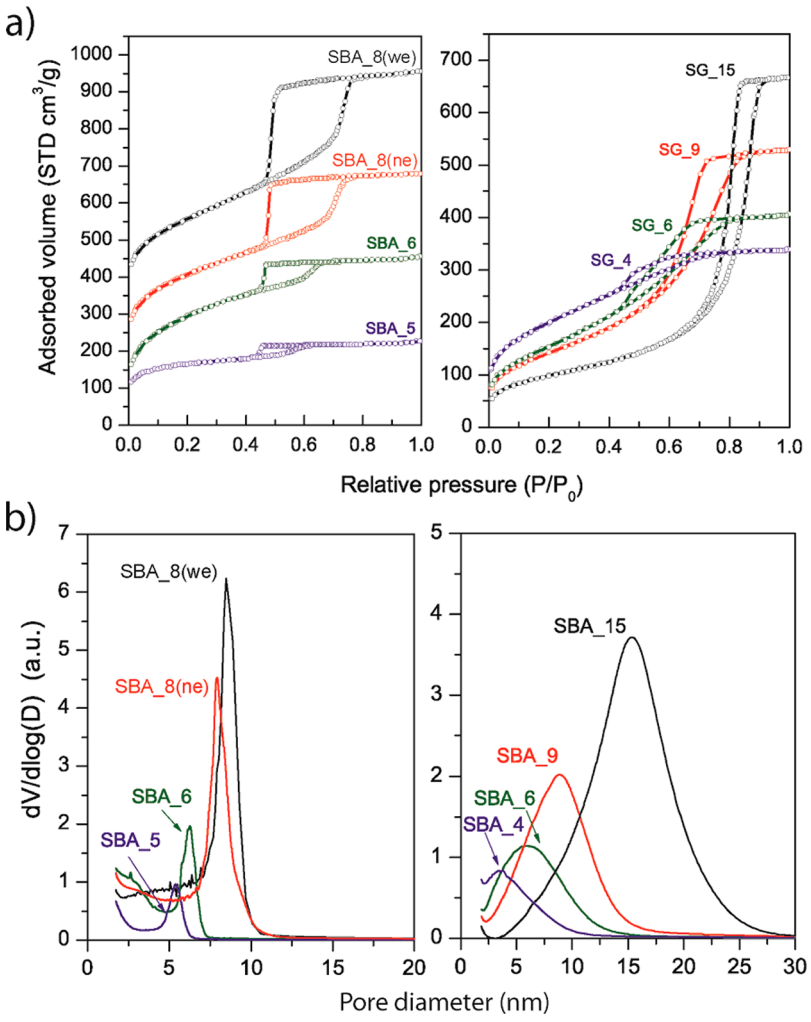

Figure 1. (a) N_2-physisorption isotherms, and (b) pore size distributions from the adsorption branches for the series of SBA-16 and SiO_2-gel support materials. For clarity, in panel (a) the isotherms for SBA_8(ne) and SBA_8(we) have been vertically offset by 150 and 300 $cm^3\ g^{-1}$, respectively.

TABLE 1. Textural Properties of the Silica Support Materials and Metal Dispersion in the Resulting CuZnO/SiO_2 Catalysts

	support porosity					catalyst metal dispersion		
support	S_{BET}[a] ($m^2\ g^{-1}$)	V_p[b] ($cm^3\ g^{-1}$)	V_{mp}[c] ($cm^3\ g^{-1}$)	cage/pore size[d] (nm)	entrance size (nm)	Cu (wt %)	d(CuO)[g] (nm)	d(Cu)[h] (nm)
SBA_5	571	0.34	0.14	5.3	2.3[e]	4.3	n.d.[i]	3.3
SBA_6	834	0.55	0.04	6.3	3.3[e]	7.8	n.d.	—
SBA_8(ne)	925	0.82	0.03	7.8	3.7[f]	9.9	7.9	4.9
SBA_8(we)	930	1.00	0.00	8.4	4.5[f]	11.9	7.3	4.8
SG_4	718	0.53	0.01	3.5	—	9.6	n.d.	—
SG_6	573	0.63	0.00	6.0	—	10.8	2.4	4.6
SG_9	522	0.82	0.00	8.8	—	10.8	4.8	6.5
SG_15	354	1.03	0.00	15.2	—	11.8	6.4	9.7

[a] B.E.T. surface area. [b] Total pore volume determined as the N_2 uptake at a relative pressure P/P_0 of 0.95. [c] Micropore volume. [d] Determined by applying the BJH method to the adsorption branch of the N_2-physisorption isotherm. [e] Determined by functionalization of the silica surface with organosilanes with different linear chain lengths combined with N_2-physisorpton (see Supplementary Figure S3). [f] Determined by applying the BJH method to the desorption branch of the Ar-physisorption isotherm. [g] Volume-averaged CuO crystallite size. [h] Surface-averaged Cu particle size after catalyst reduction as determined by HAADF-STEM. [i] n.d.: not detected.

the higher hydrothermal temperatures employed during their syntheses. SBA_8(ne) and SBA_8(we) display very similar cage diameters of 8.1 ± 0.3 nm.

Besides the cage diameter, the size of the cage entrances is a prime structural parameter of the cage-like porous materials. As desorption from the silica

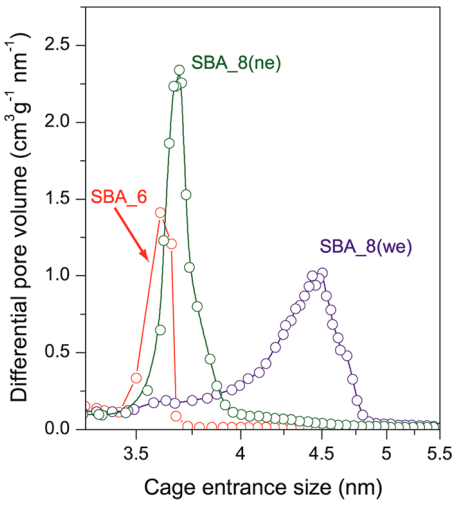

Figure 2. Cage entrance size distributions obtained by Ar-physisorption (desorption branch) for selected SBA-16 support materials.

nanocages occurs *via* cavitation in all cases, N_2-physisorption indicates cage entrances narrower than 4.7 nm.[47] Ar physisorption was applied to extend the range of quantifiable entrance sizes (Supplementary Figure S2).[48] The corresponding entrance size distributions are depicted in Figure 2. The sharp size distribution peaking at ca. 3.6 nm for SBA_6 (and SBA_5, not shown in Figure 2) corresponds to an artifact associated with the forced (steep) closure of the desorption branch at the point of Ar cavitation at 77 K. Therefore, it sets the lowest limit of the method to quantify the entrance sizes, indicating that those two materials display entrances narrower than 3.6 nm. Slightly above this limit, a mean entrance size of 3.7 nm was determined for SBA_8(ne), while wider entrances of 4.5 nm were found for SBA_8(we).

For those SBA-16 samples for which the entrance size remained out of reach for gas physisorption methods, an alternative approach based on the grafting of organic moieties with gradually increasing molecular sizes was adopted[49−52] (Supplementary Figure S3). This analysis results in mean entrance sizes of 2.3 and 3.3 nm for SBA_5 and SBA_6, respectively (Table 1).

Deposition of Nanosized CuZnO catalysts. Essential for the purpose of this study was to efficiently deposit CuZnO species exclusively inside the pores of the SiO_2 carriers. Impregnation of porous carriers with an aqueous solution of metal nitrate precursors is a preferred synthesis method due to its simplicity, cost effectiveness, and low waste production.[53] However, drying and subsequent nitrate decomposition thermal treatments often promote metal agglomeration, yielding poor metal dispersions. Recently, mechanistic insights have provided the basis to counter metal agglomeration during catalyst preparation. Louis and co-workers reported the detrimental impact of high drying temperatures (>363 K) on the ultimate metal dispersion for nitrate-derived, silica-supported Cu and Zn catalysts.[54,55] For the subsequent thermal treatment, our group has developed an effective approach to prevent metal agglomeration *via* the nitric oxide moderated nitrate decomposition.[20,44,56,57] For the $CuZn/SiO_2$ materials investigated here, thermal treatment in 2%NO/N_2 results in a low-temperature controlled hydrolysis of the metal nitrate salts, yielding a pore-confined mixed metal hydroxynitrate species (Figure S4). Further decomposition at higher temperatures in the presence of NO affords small CuO nanocrystals (7.9 nm) located exclusively in the silica pores (for details, see Figure S5 and the accompanying discussion, in the Supporting Information). These results underscore the significance of the careful design of all the elementary steps during catalyst synthesis and activation to successfully incorporate the CuZnO nanocatalysts inside the pores of the silica carrier material. Catalysts discussed hereafter were obtained by impregnation followed by vacuum drying at room temperature and nitrate decomposition in the flow of 2%NO/N_2.

Table 1 contains the Cu loading and dispersion in the series of $CuZnO/SiO_2$ catalysts. With the single-step impregnation approach applied, a rather constant pore volumetric loading of 1.75 ± 0.35 Cu atoms nm^{-3} is achieved, which corresponds to Cu weight loadings in the range of 4 to 12%. As particle growth takes place within the pores, a set of materials with a constant amount of metal per unit pore volume provides the basis for a relevant comparison in terms of nanoparticle stability. After nitrate decomposition, CuO is the only crystalline phase detected with XRD. No CuO diffractions are observed for CuZnO/SBA-16 catalysts on supports with small cages (SBA_5 and SBA_6), indicative of poor crystallinity or very small oxide crystallite sizes. For those samples showing copper oxide diffractions, the CuO crystallite size increases with increasing the cage/pore size of the support material. The absence of X-ray diffractions ascribed to Zn species evidences their amorphous character irrespective of the metal content and support material. Previous results revealed the formation of a surface Zn (hydro)silicate.[19] Similarly synthesized Cu/SBA-16 catalysts show also high metal dispersion with CuO crystallite sizes <10 nm, increasing with increasing support cage size (Supplementary Table S1).

High angle annular dark-field scanning transmission electron microscopy (HAADF-STEM) was applied to study the Cu dispersion after the reduction treatment preceding catalysis (*vide infra*, Figure 5). Generally, Cu nanoparticles are found in domains with high metal density.[19] For wide-cage CuZnO/SBA_8(ne) (and CuZnO/SBA_8(we), not shown) a bimodal Cu particle size distribution is observed, with a major contribution from particles of ca. 2 nm diameter accompanied by an additional population of particles with average sizes of 7.5−8 nm, in direct correspondence with the cage

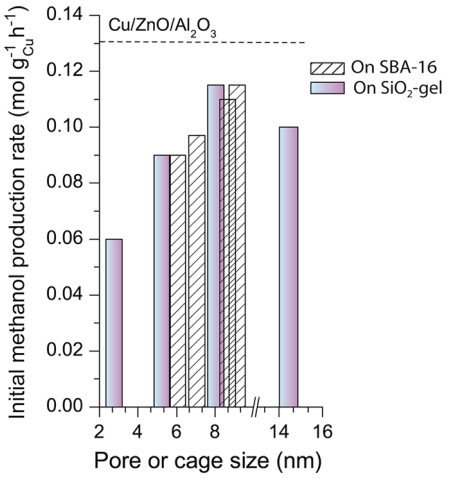

Figure 3. Copper-specific initial methanol production rate as a function of the cage/pore size for $CuZnO/SiO_2$ catalysts supported on SBA-16 mesostructures (dashed columns) and SiO_2-gel materials (full columns). Reaction conditions: T = 533 K, P = 40 bar, synthesis gas feedstock $Ar/CO_2/CO/H_2$ = 10:7:23:60 (vol), initial ($CO + CO_2$) conversion of 15−20%.

diameters of the support. This result indicates that a fraction of Cu particles grow to the size of the silica cages during reduction. Cu particle size histograms show a right-skewed log-normal character for catalysts supported on SiO_2-gel. For all the studied catalysts, the surface-averaged Cu particle size spans the range of 3−10 nm.

Catalytic Activity. The activity of the $CuZnO/SiO_2$ catalysts was evaluated under relevant methanol synthesis conditions, though at a rather high reaction temperature of 533 K to attain significant catalyst deactivation within laboratory time scales. All initial Cu mass-specific methanol production rates are comparable to, and up to 90% of, that for a benchmark $Cu/ZnO/Al_2O_3$ catalyst prepared by the conventional coprecipitation route (Figure 3). Variations in initial activity within the series of $CuZnO/SiO_2$ catalysts relate to differences in the exposed Cu surface area rather than to varying Cu surface-specific activities.[20] The lower reaction rate observed for cage/pore sizes below 8 nm is ascribed to an increasingly higher proportion of the surface of the Cu nanoparticles in contact with the silica pore walls, and hence not available for catalysis.[20] This effect might also explain that catalysts confined to cagelike pores display slightly lower initial activities than those hosted in unconstrained pores, in spite of the former containing on average smaller Cu nanoparticles. The highly curved, concave internal surface of cagelike pores likely results in a higher fraction of the Cu particle surface in direct contact with the support pore walls. As an example, CuZn/SBA_8(ne) shows a ca. 5% lower initial reaction rate than CuZn/SG_9(ne), despite the smaller particle size (4.9 nm vs 6.5 nm) of the former.

The high catalytic activities displayed by the $CuZn/SiO_2$ materials result partly from the high Cu dispersions attained through careful design of the catalyst synthesis procedure. Illustrating this, a CuZnO/SBA_8(ne) catalyst obtained by drying at 393 K followed by calcination in stagnant air (not included in Figure 3) reached only 63% of the initial activity of the NO-calcined counterpart. Another important factor is the efficient interaction with the Zn promoter species, as judged from the up to 6-fold lower initial methanol production rates obtained with Cu/SiO_2 analogues (Supplementary Figure S6). Methanol selectivities exceeded 98 C-% in all cases, with dimethyl ether being the main side product.

Earlier studies have targeted the preparation of CuZnO methanol synthesis catalysts embedded in SiO_2 matrices. Poor activities have been reported for catalysts prepared by impregnation−calcination using nitrate precursors, *e.g.* a 15-fold lower Cu-specific rate than that for a $Cu/ZnO/Al_2O_3$ benchmark catalyst.[58,59] Generally, sophisticated synthesis approaches were required to achieve small Cu nanoparticles and thereby significant catalytic activities. Grünert and co-workers devised a synthesis route based on liquid infiltration of the silica carrier with an inorganic Cu precursor and a purpose-developed organometallic Zn precursor which resulted in improved methanol formation rates.[43] Catalytic activities on the order of a coprecipitated binary Cu/ZnO catalyst were achieved by Becker *et al.* through chemical vapor deposition of Cu and Zn organic precursors on MCM-type mesoporous silicas.[42] Our results demonstrate that highly active $CuZnO/SiO_2$ catalysts can be conveniently synthesized by aqueous impregnation, based on low-cost metal nitrate precursors, by selectively depositing nanosized metal species in the porosity of the silica carriers through the NO-moderated nitrate decomposition after mild drying.

Catalyst Stability: Effect of Support Pore Size and Morphology. Figure 4a shows the gradual decrease in activity with run time for different $CuZnO/SiO_2$ catalysts. Under the applied reaction conditions, the catalytic activity drops 29−77% after 240 h on stream. N_2 physisorption analysis discards pore blockage as an explanation for the observed deactivation (Supplementary Table S2). Generally, slower deactivation is observed for catalysts supported on cagelike silicas than for those supported on SiO_2-gel materials. A reverse trend in stability would be expected based on metal particle size arguments, as on average smaller Cu nanoparticles, which are considered to be more prone to grow, are found in catalysts supported on cagelike mesostructures after reduction. Hence, this indicates the relevance of support porosity for stability. To enable comparison of the different deactivation behaviors on a quantitative basis, a common second-order deactivation law has been used to fit all the activity decay curves.[19] Figure 4b−c depict the dependence of the second-order deactivation rate constant ($k_{d,2}$) on the pore dimensions of the support materials for the two series of catalysts.

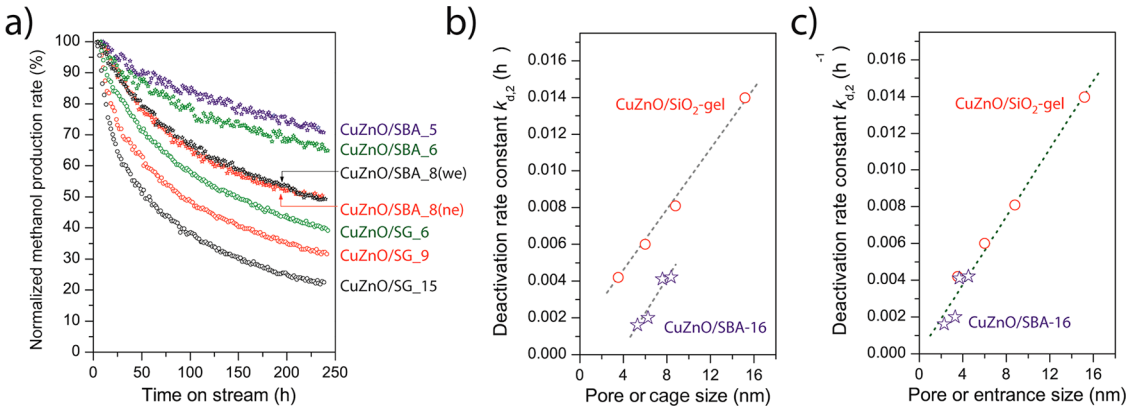

Figure 4. (a) Evolution of the normalized methanol production rate with time on stream (non-normalized deactivation curves are given as Supplementary Figure S7); dependence of the second-order deactivation rate constant with (b) the cage and pore size and (c) the entrance and pore size for CuZnO/SiO_2 catalysts supported on SBA-16 and SiO_2-gel supports, respectively. Data corresponding to CuZnO/SG_4 have not been included in panel (a) for clarity. In panel (c) the dashed line corresponds to the linear fit of all the data points. Reaction conditions: T = 533 K, P = 40 bar, synthesis gas feedstock Ar/CO_2/CO/H_2 = 10:7:23:60 (vol), initial (CO + CO_2) conversion of 15−20%.

The deactivation rate constant depends strongly on the pore size. When the widest pore characteristic dimension of the cagelike materials, *i.e.* the nanocage diameter, is considered in the comparison, two different correlations are found for the distinct pore morphologies, with deactivation rate constants 2−4 times lower for catalysts supported on SBA-16 than for the corresponding catalysts synthesized on SiO_2-gel supports (Figure 4b). In contrast, a general inverse correlation between catalyst stability and support pore size is found, which comprises both pore morphologies, when the narrowest characteristic pore dimension, *i.e.* the entrance size, is considered as the relevant porosity descriptor for cagelike silica support materials (Figure 4c).

The extent of Cu particle growth during catalysis was assessed for selected catalysts by HAADF-STEM. Figure 5 shows representative STEM micrographs along with the corresponding Cu particle size histograms for selected catalysts both prior and after their exposure to catalysis for 240 h. In all cases particle growth took place during catalysis. For catalysts supported on SBA-16, Cu particles larger than the silica cages are not observed after reaction, evidencing that cage-confinement provides an effective limit to growth. This is emphasized by the cutoff observed in the particle size distributions of the spent catalysts for sizes in correspondence with the diameter of the silica cages, as it is most clearly observed for CuZnO/SBA_8-(ne) which showed a higher growth extent (Figure 5f). Also for CuZnO/SG_9 the final Cu particle size distribution after catalysis is circumscribed to the boundaries set by the pore size distribution of the support (Figure 5i), indicating a sufficient mechanical stability of the silica pore walls and their effective role to limit particle growth.

After 10 days on-stream, the surface-averaged Cu particle size had increased 15%, 23%, and 31% for catalysts supported on SBA_5, SBA_8(ne), and SG_9, respectively. The trend is in agreement with the deactivation behavior (Figure 4), supporting that smaller entrances restrict Cu particle growth more efficiently and hence lead to improved stability. Nonetheless, the decrease in Cu surface area derived directly from the observed Cu particle growth does not fully explain on its own the activity decay registered. This result is in line with previous observations[19] and suggests that particle growth brings about supplementary contributions to catalyst deactivation which might be explained by a blockage of the metal surface by direct interaction with the silica pore walls, or a degradation of the interaction with the Zn promoter species. However, whereas deterioration of the Cu−Zn interaction upon Cu particle growth might have contributed to some extent to catalyst deactivation, consistent deactivation trends were found for analogous Cu/SiO_2 catalysts, without Zn (Supplementary Figure S6), confirming the relevance of the support pore size and morphology for Cu particle growth and catalyst stability.

Although enhanced stability has also been recently reported upon cage confinement of metal nanoparticles under conditions favoring Ostwald ripening[60] for CuZnO/SiO_2 catalysts with short distances between the Cu particles exposed to relevant methanol synthesis reaction conditions, as those reported here, we have previously reported that particle coalescence seems to contribute significantly to growth.[20] This interpretation is reinforced by the fact that improved stability is observed with the presence of narrow constraints within the porosity of the silica carrier material. Considering the average size of the Cu nanoparticles and the silica nanocages, it is unlikely that more than two Cu particles are hosted in a single cage prior to catalysis. Hence, the enhanced stability is most likely due to restricted intercage particle migration which brings about a significant metal "compartmentalization" and

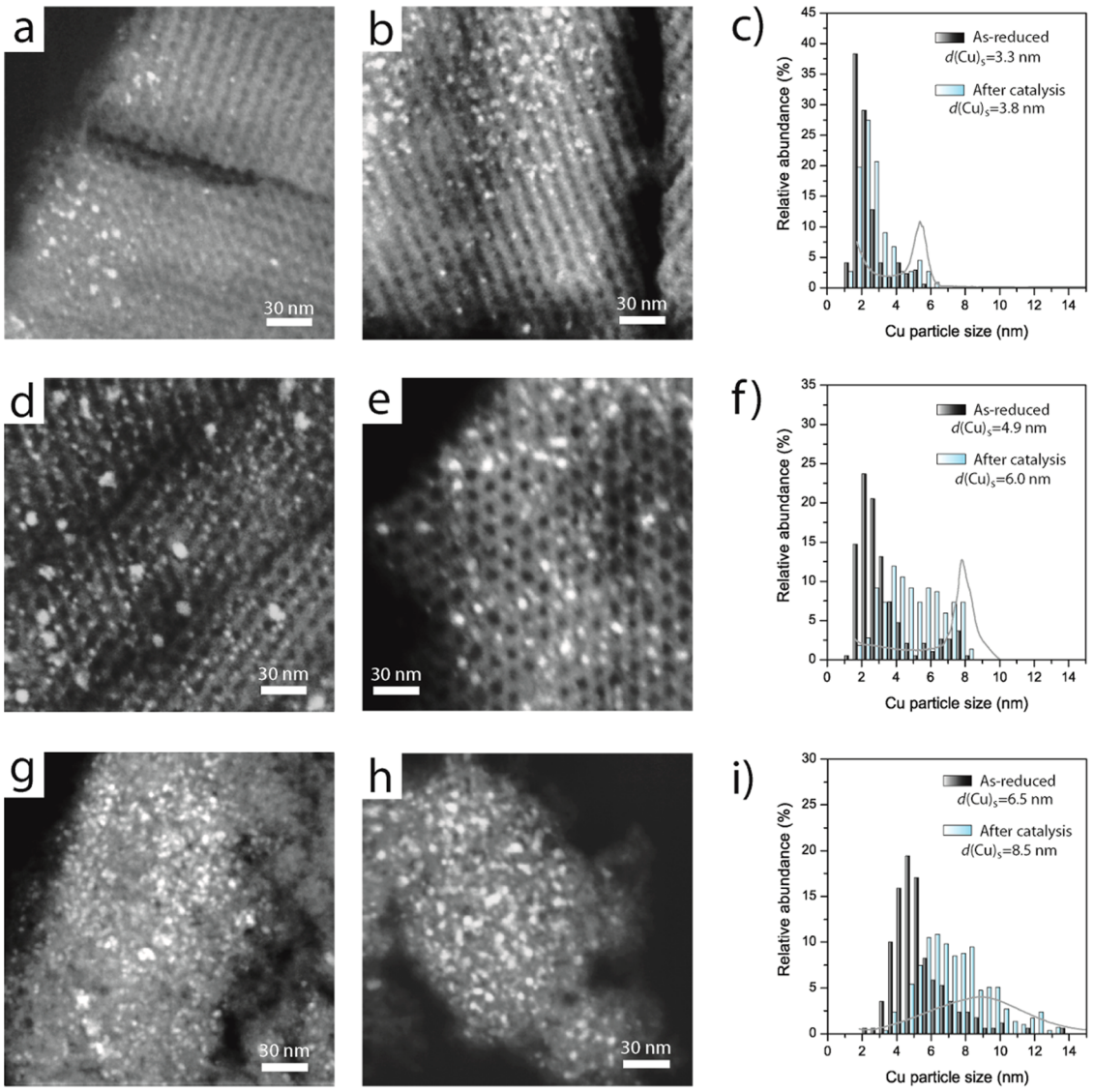

Figure 5. HAADF-STEM micrographs of ultramicrotomed sections (nominal thickness of 50 nm) and the derived Cu particle size distributions for (a–c) CuZnO/SBA_5, (d–f) CuZnO/SBA_8(ne), and (g–i) CuZnO/SG_9 before (a,d,g) and after (b,e,h) exposure to catalysis conditions for 240 h. The cage/pore size distributions of the support materials have been included as a gray line in the corresponding Cu particle size histogram plots.

limits growth *via* particle coalescence. The hampered migration of metal particles between cages might result either from a direct geometrical constraint, owing to the fact that most Cu particles in the activated catalysts are already similar in size or larger than the cage entrances, or from the energetically unfavorable displacement of the particles from the concave inner surface of the nanocages.[61] Particularly in the first case, the entrance size is anticipated to play a major role for particle stabilization, which is consistent with the direct relationship found between the catalyst stability and the size of the narrowest characteristic pore dimension of the silica host materials.

CONCLUSIONS

A series of CuZnO/SiO_2 catalysts have been synthesized by impregnation using an aqueous solution of the metal nitrate precursors. Nitric oxide assisted nitrate decomposition following vacuum drying at room temperature enables the efficient deposition of small Cu nanoparticles exclusively inside the support porosity, displaying short interparticle spacings. Under relevant methanol synthesis reaction conditions, the thus synthesized catalysts show a high initial Cu-methanol production rate, comparable to that for a reference Cu/ZnO/Al_2O_3 catalyst obtained by a conventional coprecipitation route. Confinement of the CuZnO catalysts in cagelike silica pores limits particle growth and hence improves stability with respect to catalysts supported on SiO_2-gel materials with also 3D interconnected, but unconstrained, porosity. A strong inverse relationship is found between catalyst stability and the support pore size, comprising both pore morphologies, provided the narrowest characteristic

pore dimension, *i.e.* the entrance to the nanocages for cagelike pores, is considered as the relevant porosity descriptor. Overall, our study emphasizes how advanced control over nanoscale features of porous materials enables the establishment of general and quantitative structure–performance relationships, as an efficient strategy toward the rational design of more stable and durable catalysts and other functional nanostructures in applications where metal nanoparticle growth represents a hurdle.

METHODS

Synthesis of SBA-16 Support Materials. Four different SBA-16 silica mesostructures were synthesized with varying cage and entrance sizes. These support materials are denoted as SBA_*x*(*y*), where *x* denotes the mean cage diameter in nm and, optionally, *y* is "*ne*" denoting narrow entrance or "*we*" denoting wide entrance for materials displaying essentially the same cage size.

Block-copolymers Pluronic F127 ($EO_{106}PO_{70}EO_{106}$) and Pluronic P123 ($EO_{20}PO_{70}EO_{20}$) from Sigma-Aldrich, 1-butanol (p.a., Acros), and tetraethyl ortosilicate (TEOS, ≥99%, Sigma-Aldrich) were used as received. SBA-16 silica materials with small cages (5–6 nm) were synthesized following the procedure reported by Kim *et al.*[49] using a synthesis gel with the following molar composition: 0.0016 P123/0.0037 F127/1.0 TEOS/4.4 HCl/140 H_2O. The copolymers were dissolved at room temperature in HCl/H_2O. TEOS was subsequently added dropwise under fast magnetic stirring, and the gel was aged in an oven at 308 K for 20 h under static conditions. The mixture was hydrothermally treated at 333 K (SBA_5) or 373 K (SBA_6) for 24 h. Large-cage SBA-16 silica materials were prepared using 1-butanol (BuOH) as a swelling agent at low-acid concentrations as described by Kleitz *et al.*[63] A synthesis gel with the following molar ratios was used: 0.0035 F127/1.79 BuOH/1.0 TEOS/0.91 HCl/120 H_2O. After the block-copolymer was dissolved in HCl/H_2O, 1-butanol was added and the mixture was stirred at 308 K for 1 h. Then, TEOS was added dropwise under fast magnetic stirring and the gel was aged in an oven at 35 °C for 20 h under static conditions. The mixture was further treated for 48 h at 263 K (SBA_8(ne)) or 24 h at 393 K (SBA_8(we)). The temperature and duration of the hydrothermal treatment were adjusted to obtain SBA-16 silica materials with similar cage sizes and different entrance sizes.

In all cases, after the hydrothermal treatment, the resulting solids were filtered, extensively washed with deionized water, and dried at 393 K for 10 h. Finally, the product was calcined at 813 K in a muffle oven to remove the copolymer template. For reference purposes, a series of high-purity, commercial silica gel materials (Merck and Grace) with mean pore diameters in the range of 3–15 nm were employed.

Synthesis of CuZnO/SiO_2 Catalysts. To synthesize the CuZnO/SiO_2 catalysts, the silica supports were sieved to select particles of 38–90 μm and dried at 523 K under vacuum for 2 h prior to the incorporation of the metal precursors. Then the supports were impregnated to incipient wetness using a 4 M aqueous solution of Cu and Zn nitrates (atomic ratio Cu/Zn = 65/35) in 0.1 M HNO_3 (pH < 1). After impregnation, the solids were dried for 12 h at room temperature under dynamic vacuum. Finally, the supported metal nitrate precursors were decomposed by submitting the samples to thermal treatment at 723 K for 1 h under a flow of 2%NO/N_2 (v/v). A heating rate of 2 K min^{-1} and a gas hourly space velocity (GHSV) of $1.0 \cdot 10^4$ h^{-1} were applied. Catalysts were denoted CuZnO/*x*_*y*, where *x* is SG for catalysts supported on SiO_2-gel and SBA when SBA-16 mesostructure was used as the support, and *y* denotes the pore/cage size in nm. Reference Cu/SiO_2 catalysts were also synthesized as indicated above, though a 4 M $CuNO_3 \cdot 3H_2O$ solution in 0.1 M HNO_3 was used in the impregnation step. Control materials were prepared by drying the impregnated solid in an oven at 393 K and/or calcining the dried impregnate at 723 K for 1 h in a stagnant air atmosphere, using a muffle oven.

Catalyst Characterization Methods. N_2 and Ar physisorption isotherms were measured at 77 K using a Micromeritics TriStar 3000 apparatus. Prior to analysis, the samples were treated in a N_2 flow at 523 K for 12 h. Surface areas were derived using the BET method, and the total pore volumes were based on the amount of N_2 adsorbed at a relative pressure of $P/P_0 = 0.95$. The average cage size was defined as the maximum value in the pore size distribution (PSD) derived from the physisorption results by applying the Barrett–Joyner–Halenda (BJH) model modified according to the Kruk–Jaroniec–Sayari (KJS) correction with the Harkins–Jura empirical thickness equation to the N_2 adsorption branch. The size distribution of the widest-entrance path to the cages was derived from the Ar desorption branch using the BJH model with empirically established corrections as published by Kruk *et al.*[62]

Hydrogen temperature programmed reduction (H_2-TPR) was employed to determine the Cu loading in the catalysts in an Autochem 2910 from Micromeritics as previously described. The single reduction peak at 493–533 K was integrated, and the determined H_2 consumption was ascribed to the reduction of CuO according to the stoichiometry $CuO + H_2 \rightarrow Cu + H_2O$.

X-ray diffractograms were acquired at rt in the 2θ range from 10° to 80° (step size of 0.06°, scan speed 356 s $step^{-1}$) using Co $K_{\alpha 1,2}$ radiation (λ = 1.79026 Å). The copper oxide crystallite size was estimated by applying the Scherrer equation (k = 0.9) to the (1 1 1) diffraction of CuO (2θ = 45.5). Corundum (α-Al_2O_3) was used to determine the experimental line broadening.

Bright-field transmission electron microscopy (TEM) was performed in a Tecnai 12 microscope (FEI) operated at 120 kV. High-angle annular dark-field scanning-transmission electron microscopy (HAADF-STEM) and energy dispersive X-ray spectroscopy (EDX) were performed in a Tecnai 20FEG microscope (FEI) operated at 200 kV. As-reduced or spent catalysts were passivated by controlled exposure to oxygen at rt and stored in a glovebox (<1 ppm O_2) until specimen preparation for microscopy. Then the powdered catalysts were embedded in an epoxy resin (Epofix, EMS) and cured at rt for 72 h. The embedded specimens were then cut into ultrathin sections (nominal thickness of 50 nm) using a Diatome 35° diamond knife mounted on a Reichert-Jung Ultracut microtome, and the sections were collected on carbon-coated Cu TEM grids (200 mesh, Agar Scientific). Cu particle size histograms were generated by counting at least 200 particles.

Catalysis. Methanol synthesis tests were performed in a fixed-bed stainless steel reactor. The catalysts were pressed into pellets, crushed, and sieved to select particles in the 0.42–0.63 mm size range. The catalyst bed consisted of 0.2–0.5 g of catalyst diluted with SiC granules (0.25–0.42 mm) in a ca. 1:1 volume ratio, in order to achieve plug-flow isothermal conditions. Prior to catalysis, the catalyst was reduced *in situ* at 523 K for 150 min (heating ramp of 2 K min^{-1}) under a flow of 20 vol % H_2/Ar. After reduction, the reactor was cooled down to 373 K and flushed with a synthesis gas mixture (Ar/CO_2/CO/H_2 = 10:7:23:60, vol.) for 30 min. The synthesis gas mixture was fed from a pressurized gas-mixture cylinder (Linde) and purified using a metal carbonyl trap containing H-USY zeolite (CBV-780 from Zeolyst Int., 0.5–1.5 mm) situated upstream of the reactor. The pressure was gradually increased to 40 bar, and then the reactor was heated up to the reaction temperature of 533 K (2 K min^{-1}). The gas space velocity was adjusted to achieve initial (CO + CO_2) conversions of 15–20%. The gas flow leaving the reactor was decompressed and periodically injected into a Varian 450 gas chromatograph (GC) equipped with TCD and FID detectors. Product flow rates were quantified using Ar as the internal standard. Deactivation rate constants were derived by fitting the activity profiles (normalized methanol production rate *vs*

time on stream) with a second-order deactivation rate law for reaction times of 25−240 h, as detailed elsewhere.[20]

Conflict of Interest: The authors declare no competing financial interest.

Supporting Information Available: SEM micrographs and argon physisorption isotherms of SBA-16 mesostructured supports; details on the determination of the entrance size in SBA-16 supports by grafting of organic molecules; additional XRD and TEM data on the CuZn/SBA-16 catalysts; catalytic performance of Cu/SiO_2 catayst; N_2 physisorption data for selected $CuZn/SiO_2$ catalysts after the catalytic tests. This material is available free of charge *via* the Internet at http://pubs.acs.org.

Acknowledgment. This material is based upon work supported as part of the Center for Atomic-Level Catalyst Design, an Energy Frontier Research Center funded by the U.S. Department of Energy, Office of Science, Office of Basic Energy Sciences under Award Number DE-SC0001058. Additional support from The Netherlands Organization for Scientific Research through the NWO-TOP (K.P.d.J.) and NWO-Vici (P.E.d.J.) programs is also acknowledged. The authors are grateful to Grace for kindly providing the silica gel supports. R. van Zwienen and J. D. Meeldijk (Utrecht University) are acknowledged for assistance with the high-pressure catalytic setup and involvement in the HAADF-STEM experiments, respectively. T. M. Eggenhuisen is acknowledged for her involvement in Ar physisorption. E. van Donselaar and R. Mesman (Utrecht University) are thanked for ultramicrotomy instructions. The Electron Microscopy Unit at Utrecht University is acknowledged for their excellent facilities.

REFERENCES AND NOTES

1. *Handbook of Heterogeneous Catalysis*, Ertl, G., Knözinger, H., Schüth, F., Weitkamp, J., Eds.; Wiley-VCH: Weinheim, 2008.
2. Wynblatt, P.; Gjostein, N. A. Supported Metal Crystallites. *Prog. Solid State Chem.* **1975**, *9*, 21–58.
3. Bartholomew, C. H. Mechanisms of Catalyst Deactivation. *Appl. Catal. A Gen.* **2001**, *212*, 17–60.
4. Moulijn, J. A.; van Diepen, A. E.; Kapteijn, F. Catalyst Deactivation: Is it Predictable?-What to Do?. *Appl. Catal., A* **2001**, *212*, 3–16.
5. Valden, M.; Lai, X.; Goodman, D. W. Onset of Catalytic Activity of Gold Clusters on Titania with the Appearance of Nonmetallic Properties. *Science* **1998**, *281*, 1647–1650.
6. Van Santen, R. A. Complementary Structure Sensitive and Insensitive Catalytic Relationships. *Acc. Chem. Res.* **2009**, *42*, 57–66.
7. Bezemer, L.; Bitter, J. H.; Kuipers, H. P. C. E.; Oosterbeek, H.; Holewijn, J. E.; Xu, X.; Kapteijn, F.; Van Dillen, A. J.; de Jong, K. P. Cobalt Particle Size Effects in the Fischer−Tropsch Reaction Studied with Carbon Nanofiber Supported Catalysts. *J. Am. Chem. Soc.* **2006**, *128*, 3956–3964.
8. Hughes, M. D.; Xu, Y. J.; Jenkins, P.; McMorn, P.; Landon, P.; Enache, D. I.; Carley, A. F.; Attard, G. A.; Hutchings, G. J.; King, F.; Stitt, E. H.; Johnston, P.; Griffin, K.; Kiely, C. J. Tunable Gold Catalysts for Selective Hydrocarbon Oxidation under Mild Conditions. *Nature* **2005**, *437*, 1132–1135.
9. Torres Galvis, H. M.; Bitter, J. H.; Davidian, T.; Ruitenbeek, M.; Dugulan, A. I.; de Jong, K. P. Iron Particle Size Effects for Direct Production of Lower Olefins from Synthesis Gas. *J. Am. Chem. Soc.* **2012**, *134*, 16207–16215.
10. Boronat, M.; Concepción, P.; Corma, A.; González, S.; Illas, F.; Serna, P. A Molecular Mechanism for the Chemoselective Hydrogenation of Substituted Nitroaromatics with Nanoparticles of Gold on TiO_2 Catalysts: A Cooperative Effect between Gold and the Support. *J. Am. Chem. Soc.* **2007**, *129*, 16230–16237.
11. Prieto, G.; Concepción, P.; Martínez, A.; Mendoza, E. New Insights Into the Role of the Electronic Properties of Oxide Promoters in Rh-Catalyzed Selective Synthesis of Oxygenates from Synthesis Gas. *J. Catal.* **2011**, *280*, 274–288.
12. López-Haro, M.; Cíes, J. M.; Trasobares, S.; Pérez-Omil, J. A.; Delgado, J. J.; Bernal, S.; Bayle-Guillemaud, P.; Stéphan, O.; Yoshida, K.; Boyes, E. D.; Gai, P. L.; Calvino, J. J. Imaging Nanostructural Modifications Induced by Electronic Metal-Support Interaction Effects at Au/Cerium-Based Oxide Nanointerfaces. *ACS Nano* **2012**, *6*, 6812–6820.
13. Cao, A.; Veser, G. Exceptional High-Temperature Stability Through Distillation-like Self-Stabilization in Bimetallic Nanoparticles. *Nat. Mater.* **2010**, *9*, 75–81.
14. Farmer, J. A.; Campbell, C. T. Ceria Maintains Smaller Metal Catalyst Particles by Strong Metal-Support Bonding. *Science* **2010**, *239*, 933–936.
15. Wang, Y.; Van de Vyver, S.; Sharma, K.; Román-Leshkov, Y. Insights into the Stability of Gold Nanoparticles Supported on Metal Oxides for the Base-Free Oxidation of Glucose to Gluconic Acid. *Green Chem.* **2014**, *16*, 719–726.
16. Arnal, P. M.; Comotti, M.; Schüth, F. High-Temperature-Stable Catalysts by Hollow Sphere Encapsulation. *Angew. Chem., Int. Ed.* **2006**, *45*, 8224–8227.
17. Joo, S. H.; Park, J. Y.; Tsung, C. K.; Yamada, Y.; Yang, P.; Somorjai, G. A. Thermally Stable Pt/Mesoporous Silica Core−Shell Nanocatalysts for High-Temperature Reactions. *Nat. Mater.* **2009**, *8*, 126–131.
18. Lu, J.; Fu, B.; Kung, M. C.; Xiao, G.; Elam, J. W.; Kung, H. H.; Stair, P. C. Coking- and Sintering-Resistant Palladium Catalysts Achieved Through Atomic Layer Deposition. *Science* **2012**, *335*, 1205–1208.
19. Prieto, G.; Zecevic, J.; Friedrich, H.; de Jong, K. P.; de Jongh, P. E. Towards Stable Catalysts by Controlling Collective Properties of Supported Metal Nanoparticles. *Nat. Mater.* **2013**, *12*, 34–39.
20. Prieto, G.; Meeldijk, J. D.; de Jong, K. P.; de Jongh, P. E. Interplay between Pore Size and Nanoparticle Spatial Distribution: Consequences for the Stability of CuZn/SiO_2 Methanol Synthesis Catalysts. *J. Catal.* **2013**, *303*, 31–40.
21. Cao, A.; Lu, R.; Veser, G. Stabilizing Metal Nanoparticles for Heterogeneous Catalysis. *Phys. Chem. Chem. Phys.* **2010**, *12*, 13499–13510.
22. Wang, J.; Lu, A.-H.; Li, M.; Zhang, W.; Chen, Y.-S.; Tian, D.-X.; Li, W.-C. Thin Porous Alumina Sheets as Supports for Stabilizing Gold Nanoparticles. *ACS Nano* **2013**, *7*, 4902–4910.
23. Ruckenstein, E.; Pulvermacher, B. Effect of the Pore Size on the Aging of Supported Metals. *J. Catal.* **1975**, *37*, 416–423.
24. Richardson, J. T.; Propp, J. L. Pore Size Effects on Sintering of Ni/Al_2O_3 Catalysts. *J. Catal.* **1986**, *98*, 457–467.
25. Sun, J.; Ma, D.; Zhang, H.; Liu, X.; Han, X.; Bao, X.; Weinberg, G.; Pfänder, N.; Su, D. Toward Monodispersed Silver Nanoparticles with Unusual Thermal Stability. *J. Am. Chem. Soc.* **2006**, *128*, 15756–15764.
26. Bore, M. T.; Pham, H. N.; Switzer, E. E.; Ward, T. L.; Fukuoka, A.; Datye, A. K. The Role of Pore Size and Structure on the Thermal Stability of Gold Nanoparticles within Mesoporous Silica. *J. Phys. Chem. B* **2005**, *109*, 2873–2880.
27. Zhao, D. Y.; Huo, Q. S.; Feng, J. L.; Chmelka, B. F.; Stucky, G. D. Nonionic Triblock and Star Diblock Copolymer and Oligomeric Surfactant Syntheses of Highly Ordered, Hydrothermally Stable, Mesoporous Silica Structures. *J. Am. Chem. Soc.* **1998**, *120*, 6024–6036.
28. Yu, C. Z.; Yu, Y. H.; Zhao, D. Y. Highly Ordered Large Caged Cubic Mesoporous Silica Structures Templated by Triblock PEO-PBO-PEO Copolymer. *Chem. Commun.* **2000**, 575–576.
29. Fan, J.; Yu, C. Z.; Gao, T.; Lei, J.; Tian, B. Z.; Wang, L. M.; Luo, Q.; Tu, B.; Zhou, W. Z.; Zhao, D. Y. Cubic Mesoporous Silica with Large Controllable Entrance Sizes and Advanced Adsorption Properties. *Angew. Chem., Int. Ed.* **2003**, *42*, 3146–3150.
30. Matos, J. R.; Kruk, M.; Mercuri, L. P.; Jaroniec, M.; Zhao, L.; Kamiyama, T.; Terasaki, O.; Pinnavaia, T. J.; Liu, Y. Ordered Mesoporous Silica with Large Cage-Like Pores: Structural Identification and Pore Connectivity Design by Controlling the Synthesis Temperature and Time. *J. Am. Chem. Soc.* **2003**, *125*, 821–829.
31. Li, L. Y.; King, D. L.; Liu, J.; Huo, Q. S.; Zhu, K. K.; Wang, C. M.; Gerber, M.; Stevens, D.; Wang, Y. Stabilization of Metal

Nanoparticles in Cubic Mesostructured Silica and Its Application in Regenerable Deep Desulfurization of Warm Syngas. *Chem. Mater.* **2009**, *21*, 5358–5364.
32. Hao, Y.; Chong, Y.; Li, S.; Yang, H. Controlled Synthesis of Au Nanoparticles in the Nanocages of SBA-16: Improved Activity and Enhanced Recyclability for the Oxidative Esterification of Alcohols. *J. Phys. Chem. C* **2012**, *116*, 6512–6519.
33. Li, X.; Liu, X.; Yang, Y.; Zhao, J.; Li, C.; Yang, Q. Entrapment of Metal Nanoparticles within Nanocages of Mesoporous Silicas Aided by Co-Surfactants. *J. Mater. Chem.* **2012**, *22*, 21045–21050.
34. *Concepts of Modern Catalysis and Kinetics*; Chorkendorff, I., Niemantsverdriet, H., Eds.; Wiley-VCH: Weinheim, 2003.
35. *Beyond Oil and Gas: The Methanol Economy*; Olah, G. A., Goeppert, A., Surya Prakash, G. K., Eds.; Wiley-VCH: Weinheim, 2009.
36. Twigg, M. V.; Spencer, M. S. Deactivation of Copper Metal Catalysts for Methanol Steam Reforming and Methanol Synthesis. *Top. Catal.* **2003**, *22*, 191–203.
37. Rasmussen, D. B.; Janssens, T. V. W.; Temel, B.; Bligaard, T.; Hinnemann, B.; Helveg, S.; Sehested, J. The Energies of Formation and Mobilities of Cu Surface Species on Cu and ZnO in Methanol and Water Gas Shift Atmospheres Studied by DFT. *J. Catal.* **2012**, *293*, 205–214.
38. Baltes, C.; Vukojević, S.; Schüth, F. Correlations Between Synthesis, Precursor, and Catalyst Structure and Activity of a Large Set of $CuO/ZnO/Al_2O_3$ Catalysts for Methanol Synthesis. *J. Catal.* **2008**, *258*, 334–344.
39. Behrens, M.; Studt, F.; Kasatjin, I.; Kühl, S.; Hävecker, M.; Abild-Pedersen, K.; Zander, S.; Girgsdies, F.; Kurr, P.; Kniep, B.-L.; Tovar, M.; Fischer, R. W.; Nørskov, J. K.; Schlögl, R. The Active Site of Methanol Synthesis over $Cu/ZnO/Al_2O_3$ Industrial Catalysts. *Science* **2012**, *336*, 893–897.
40. Prieto, G.; de Jong, K. P.; de Jongh, P. E. Towards "Greener" Catalyst Manufacture: Reduction of Wastewater from the Preparation of $Cu/ZnO/Al_2O_3$ Methanol Synthesis Catalysts. *Catal. Today* **2013**, *215*, 142–151.
41. Jansen, W. P. A.; Beckers, J.; van der Heuvel, J. C.; van der Gon, A. W. D.; Bliek, A.; Brongersma, H. H. Dynamic Behavior of the Surface Structure of $Cu/ZnO/SiO_2$ Catalysts. *J. Catal.* **2002**, *210*, 229–236.
42. Becker, R.; Parala, H.; Hipler, F.; Tkachenko, O. P.; Klementiev, K. V.; Grünert, W.; Wilmer, H.; Hinrichsen, O.; Muhler, M.; Birkner, A.; Wöll, C.; Schäfer, S.; Fischer, R. A. MOCVD-Loading of Mesoporous Siliceous Matrices with Cu/ZnO: Supported Catalysts for Methanol Synthesis. *Angew. Chem., Int. Ed.* **2004**, *43*, 2839–2842.
43. Van den Berg, M. W. E.; Polarz, S.; Tkachenko, O. P.; Klementiev, K. V.; Bandyopadhyay, M.; Khodeir, L.; Gies, H.; Muhler, M.; Grünert, W. Cu/ZnO Aggregates in Siliceous Mesoporous Matrices: Development of a New Model Methanol Synthesis Catalyst. *J. Catal.* **2006**, *241*, 446–455.
44. Munnik, P.; Wolters, M.; Gabrielsson, A.; Pollington, S. D.; Headdock, G.; Bitter, J. H.; de Jongh, P. E; de Jong, K. P. Copper Nitrate Redispersion to Arrive at Highly Active Silica Supported Copper Catalysts. *J. Phys. Chem. C* **2011**, *115*, 14698–14706.
45. Sing, K. S. W.; Williams, R. T. Physisorption Hysteresis Loops and the Characterization of Nanoporous Materials. *Adsorpt. Sci. Technol.* **2004**, *22*, 773–782.
46. Ravikovitch, P. I.; Neimark, A. V. Density Functional Theory of Adsorption in Spherical Cavities and Pore Size Characterization of Templated Nanoporous Silicas with Cubic and Three-Dimensional Hexagonal Structures. *Langmuir* **2002**, *18*, 1550–1560.
47. Eggenhuisen, T. M.; Prieto, G.; Talsma, H.; de Jong, K. P.; de Jongh, P. E. Entrance Size Analysis of Silica Materials with Cagelike Pore Structure by Thermoporometry. *J. Phys. Chem. C* **2012**, *116*, 23383–23393.
48. Kruk, M.; Jaroniec, M. Argon Adsorption at 77 K as a Useful Tool for the Elucidation of Pore Connectivity in Ordered Materials with Large Cagelike Mesopores. *Chem. Mater.* **2003**, *15*, 2942–2949.
49. Kim, T.-W.; Ryoo, R.; Kruk, M.; Gierszal, K. P.; Jaroniec, M.; Kamiya, S.; Terasaki, O. Tailoring the Pore Structure of SBA-16 Silica Molecular Sieve Through the Use of Copolymer Blends and Control of Synthesis Temperature and Time. *J. Phys. Chem. B* **2004**, *108*, 11480–11489.
50. Antonchshuk, V.; Kruk, M.; Jaroniec, M. Surface Modifications of Cage-like and Channel-like Mesopores and Their Implications for Evaluation of Sizes of Entrances to Cage-like Mesopores. *J. Phys. Chem. B* **2003**, *107*, 11900–11906.
51. Kruk, M.; Antonchshuk, V.; Matos, J. R.; Mercuri, L. P.; Jaroniec, M. Determination and Tailoring the Pore Entrance Size in Ordered Silicas with Cage-like Mesoporous Structures. *J. Am. Chem. Soc.* **2002**, *124*, 768–769.
52. Shakeri, M.; Klein Gebbink, R. J. M.; de Jongh, P. E.; de Jong, K. P. Control and Assessment of Plugging of Mesopores in SBA-15 Materials. *Microporous Mesoporous Mater.* **2013**, *170*, 340–345.
53. *Synthesis of Solid Catalysts*; de Jong, K. P., Ed.; Wiley-VCH: Weinheim, 2009.
54. Chouillet, C.; Villain, F.; Kermarec, M.; Lauron-Pernot, H.; Louis, C. Relevance of the Drying Step in the Preparation by Impregnation of Zn/SiO_2 Supported Catalysts. *J. Phys. Chem. B* **2003**, *107*, 3565–3575.
55. Catillon-Mucherie, S.; Ammari, F.; Krafft, J.-M.; Lauron-Pernot, H.; Touroude, R.; Louis, C. Preparation of Coimpregnated $Cu-Zn/SiO_2$ Catalysts: Influence of the Drying Step on Metallic Particle Size and on Cu^0-Zn^{II} Interactions. *J. Phys. Chem. C* **2007**, *111*, 11619–11626.
56. Sietsma, J. R. A.; Meeldijk, J. D.; den Breejen, J. P.; Versluijs-Helder, M.; van Dillen, A. J.; de Jongh, P. E.; de Jong, K. P. The Preparation of Supported NiO and Co_3O_4 Nanoparticles by the Nitric Oxide Controlled Thermal Decomposition of Nitrates. *Angew. Chem., Int. Ed.* **2007**, *46*, 4547–4549.
57. Wolters, M.; Munnik, P.; Bitter, J. H.; de Jongh, P. E.; de Jong, K. P. How NO Affects Nickel and Cobalt Nitrates at Low Temperatures to Arrive at Highly Dispersed Silica-Supported Nickel and Cobalt Catalysts. *J. Phys. Chem. C* **2011**, *115*, 3332–3339.
58. Okabe, K.; Sayama, K.; Matsubayashi, N.; Shimomura, K.; Arakawa, H. Selective Hydrogenation of Carbon Dioxide to Methanol on $Cu-ZnO/SiO_2$ Catalysts Prepared by Alkoxide Method. *Bull. Chem. Soc. Jpn.* **1992**, *65*, 2520–2525.
59. García-Trenco, A.; Martínez, A. A Simple and Efficient Approach to Confine Cu/ZnO Methanol Synthesis Catalysts in the Ordered Mesoporous SBA-15 Silica. *Catal. Today* **2013**, *215*, 152–161.
60. Yan, X.; Wang, X.; Tang, Y.; Ma, G.; Zou, S.; Li, R.; Peng, X.; Dai, S.; Fan, J. Unusual Loading-Dependent Sintering-Resistant Properties of Gold Nanoparticles Supported within Extra-Large Mesopores. *Chem. Mater.* **2013**, *25*, 1556–1563.
61. Ahn, T.-M.; Tien, J. K. Coarsening Kinetics of Platinum Particles on Curved Oxide Substrates. *J. Catal.* **1980**, *66*, 335–346.
62. Kruk, M.; Jaroniec, M. Determination of Mesopore Size Distributions from Argon Adsorption Data at 77 K. *J. Phys. Chem. B* **2002**, *106*, 4732–4739.
63. Kleitz, F.; Solovyov, L. A.; Anilkumar, G. M.; Choi, S. H.; Ryoo, R. Transformation of Highly Ordered Large Pore Silica Mesophases (Fm3m, Im3m and p6mm) in a Ternary Triblock Copolymer-Butanol-Water System. *Chem. Commun.* **2004**, 1536–1537.